JACS Au
AN OPEN ACCESS JOURNAL OF THE AMERICAN CHEMICAL SOCIETY

pubs.acs.org/jacsau

Article

Three States Involving Vibronic Resonance is a Key to Enhancing Reverse Intersystem Crossing Dynamics of an Organoboron-Based Ultrapure Blue Emitter

Inkoo Kim, Kwang Hyun Cho, Soon Ok Jeon, Won-Joon Son,* Dongwook Kim,* Young Min Rhee,* Inkook Jang, Hyeonho Choi, and Dae Sin Kim

Cite This: *JACS Au* 2021, 1, 987–997

Read Online

ACCESS | Metrics & More | Article Recommendations | Supporting Information

ABSTRACT: The recently developed narrow-band blue-emitting organoboron chromophores based on the multiple-resonance (MR) effect have now become one of the most important components for constructing efficient organic light emitting diodes (OLEDs). While they basically emit through fluorescence, they are also known for showing substantial thermally activated delayed fluorescence (TADF) even with a relatively large singlet−triplet gap (ΔE_{ST}). Indeed, understanding the reverse intersystem crossing (RISC) dynamics behind this peculiar TADF will allow judicious molecular designs toward achieving better performing OLEDs. Explaining the underlying nonadiabatic spin-flip mechanism, however, has often been equivocal, and how the sufficiently fast RISC takes place even with the sizable ΔE_{ST} and vanishingly small spin−orbit coupling is not well understood. Here, we show that a vibronic resonance, namely the frequency matching condition between the vibration and the electronic energy gap, orchestrates three electronic states together and this effect plays a major role in enhancing RISC in a typical organoboron emitter. Interestingly, the mediating upper electronic state is quite high in energy to an extent that its thermal population is vanishingly small. Through semiclassical quantum dynamics simulations, we further show that the geometry dependent non-Condon coupling to the upper triplet state that oscillates with the frequency $\Delta E_{ST}/\hbar$ is the main driving force behind the peculiar resonance enhancement. The existence of an array of vibrational modes with strong vibronic rate enhancements provides the ability to sustain efficient RISC over a range of ΔE_{ST} in defiance of the energy gap law, which can render the MR-emitters peculiar in comparison with more conventional donor−acceptor type emitters. Our investigation may provide a new guide for future blue emitting molecule developments.

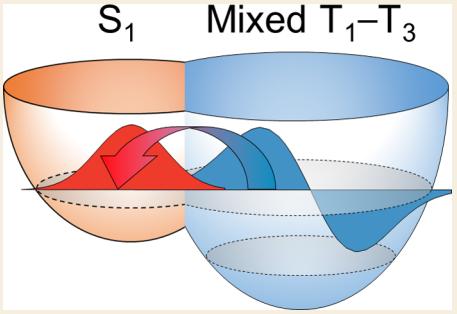

KEYWORDS: *thermally activated delayed fluorescence, multiple-resonance effect, spin−vibronic coupling, vibronic resonance, exciton transfer, coherence*

INTRODUCTION

Thermally activated delayed fluorescence (TADF) has recently emerged as a promising and pragmatic alternative to more traditional phosphorescence in the fabrication of efficient organic light emitting diodes (OLEDs).[1−4] Via triplet-to-singlet upconversion, so-called reverse intersystem crossing (RISC), TADF permits singlet emission of nearly 100% internal quantum efficiency (IQE) in OLEDs. Due to considerably weak spin−orbit couplings (SOCs) in purely organic emitters, an important parameter for TADF performance has been the energy gap between the singlet and the triplet excited states ($\Delta E_{ST} \equiv E_{S_1} - E_{T_1}$), which is related to the exchange interaction K between electrons in the frontier orbitals with $\Delta E_{ST} \simeq 2K$.[5] In this regard, conventional TADF emitters often adopt the donor−acceptor (DA) structure for spatial separation of the frontier orbitals, thereby reducing K and ΔE_{ST}. However, such DA-type emitters have inherently a dominant charge transfer character in the S_1 state. Therefore, they entail broad emission features, typically with a full-width-at-half-maximum (fwhm) > 50 nm,[6] resulting in low color purity. This aspect has indeed been one of the major hurdles to overcome for commercialization. For instance, the fwhm of the blue emission spectrum from the latest OLED display is ∼30 nm,[7] and meeting this specification will require to implement a narrow-band color filter. This will inescapably compromise the efficiency and damage the enhanced performance via TADF. Of course, this drawback will be especially serious for battery powered displays.

With regard to achieving high color purity in the blue region, the molecular design concept that arose recently by utilizing the

Received: April 26, 2021
Published: June 3, 2021

https://doi.org/10.1021/jacsau.1c00179
JACS Au 2021, 1, 987–997

multiple-resonance (MR) effect is indeed revolutionary and has already attracted significant attention.[8−11] It is realized by placing electron-donating nitrogen atoms at para-positions to a central electron-accepting boron atom in a π-conjugation scaffold as in 5,9-diphenyl-5,9-diaza-13b-boranaphtho[3,2,1-de]anthracene (DABNA, Figure 1).[8] Hence, the distributions

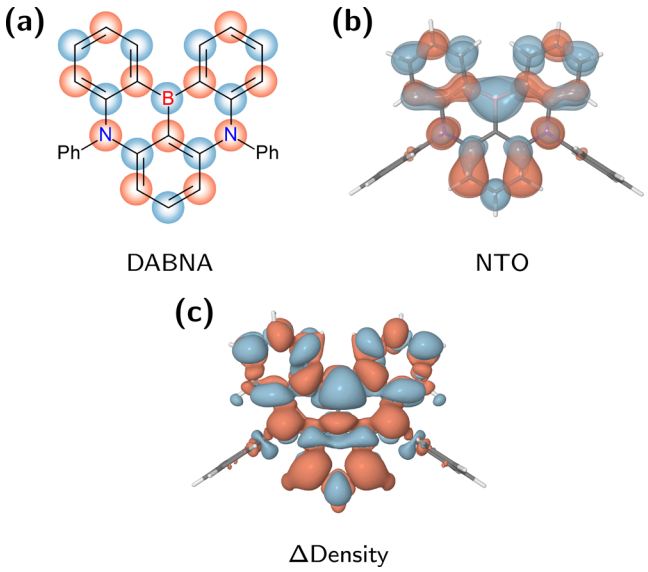

Figure 1. Narrow-band blue TADF emitter, DABNA. (a) Chemical structure with an illustration of the multiple-resonance effect (HOMO/LUMO in red/blue). (b) Hole/particle wave functions shown in red/blue, as represented by the natural transition orbitals from ω*B97X calculations. (c) Difference density plot upon S_0−S_1 excitation calculated at the SCS-ADC(2) level where the decreased/increased electron density is shown in red/blue. Notice that the transition densities include correlation effects from double excitation terms and appear somewhat differently from b.

of the highest-occupied molecular orbital (HOMO) and the lowest-unoccupied molecular orbital (LUMO) alternate within the same rigid molecular unit. As a result, a relatively fast emission ($>10^7$ s^{-1}) with an ultrapure blue spectrum (fwhm < 30 nm) results, owing to the local-excitation character and the structural rigidity of the S_1 state.

Interestingly, in MR-type emitters, although the spin−orbit coupling (SOC) between the S_1 and the T_1 states is insignificantly small and ΔE_{ST} is non-negligibly large, it is known that the RISC process also participates in generating the S_1 state during electroluminescence. While the ensuing delayed fluorescence is not remarkably swift (e.g., $\sim 10^4$ s^{-1} for DABNA[8]), the existence of this noticeable amount of TADF is important in many respects. Indeed, the RISC process not only improves the light emitting efficiency but suppresses exciton quenching (e.g., triplet−triplet annihilation and triplet−polaron quenching), while also helping the emitters remain chemically intact during the shortened T_1 state lifetime.[12] From this perspective, understanding the molecular factors behind RISC of MR-TADF emitters is of central importance to ultimately improve their excited state behaviors. However, RISC processes are generally nonradiative and nonadiabatic in nature, and accordingly, experimental and computational assessments tend to be notoriously difficult. Even greater complications are added to already-difficult computations when vibronic contributions to RISC dynamics in the form of spin−vibronic coupling are considered,[13−15] requiring a model that can handle this complex state mixing.[16,17] Recently, researchers have been actually tackling this difficult but important system theoretically.[15,18,19] For example, Northey and Penfold[15] employed the multiconfiguration time-dependent Hartree (MCTDH) quantum dynamics simulation method with a model Hamiltonian derived from the time-dependent density functional theory (TDDFT) to highlight the importance of the spin−vibronic mechanism in the ISC process from S_1 to T_1 and T_2, facilitated by nonadiabatic coupling within the singlet manifold. However, they could not observe S_1−T_1 ISC even with a sizable SOC between the two states, likely due to the overestimation of ΔE_{ST} from TDDFT (~0.6 eV) and an accidental quasi-degeneracy between S_1 and T_2. Although some spatial separation of the frontier orbitals occurs due to the alternating HOMO/LUMO distribution, the relatively small ΔE_{ST} of an MR-type emitter (<0.2 eV) is induced mainly by higher-order electron correlations.[19−21] Pershin et al.[19] employed a high level *ab initio* method to correctly investigate the theoretical origin of the reduced ΔE_{ST} in DABNA by explicitly considering the electron correlation effects that renders the local density rearrangement in spatially alternating HOMO−LUMO regions. In fact, achieving a correct energy gap structure is important not just for estimating the S_1−T_1 gap. If the T_1 energy is underestimated or the S_1 energy is overestimated, the close-by T_2 state[15] or even T_3 state[18] may mistakenly get into energetic resonance with S_1, rendering the T_2−S_1 or T_3−S_1 intersystem crossing (ISC) estimated to be unphysically too fast. Such artifacts will of course distort the prediction on the interconversion kinetics among all involved electronic states. Therefore, one can easily imagine that combining high level *ab initio* methods and kinetics and/or dynamics simulation tools will be important in unraveling the processes that are happening in DABNA.

In this work, with such purposes in our mind, we unravel the RISC dynamics of DABNA as a prototype of an ultrapure blue MR-emitter with TADF. Based on high-level quantum chemical calculations, we first evaluate the RISC rate constant (k_{RISC}) through Fermi's golden rule between T_1 and S_1 by perturbatively expanding the two involved states within the full singlet and triplet spin manifolds. We also perform semiclassical quantum dynamics simulations to investigate a superexchange behavior in its RISC. Then, by comparing with DA emitters, we discuss distinctive characteristics in the RISC of DABNA, where the spin crossover in a range of ΔE_{ST} is effectively mediated by successive and overlapping appearances of the spin−vibronic enhancements provided by an array of vibrational modes. This characterization leads to a new design rule for the development of efficient MR-TADF emitters.

RESULTS AND DISCUSSION

Reverse Intersystem Crossing Rate

We reiterate that low-cost correlated excited state methods such as linear response TDDFT do not predict ΔE_{ST} well for DABNA, as electron correlations in the form of double excitations tend to reduce the gap.[21] We therefore employed a relatively higher level of theory, SCS-CC2/TZVPP//SCS-ADC(2)/SVP. Its spin-component scaling can also improve the accuracy of the excited state potential energy surface[22] and, therefore, aids the normal-mode analyses toward obtaining mode-mixing rotations and displacements between pairs of excited states.[23] In addition, reliably calculating the energy gaps

https://doi.org/10.1021/jacsau.1c00179
JACS Au 2021, 1, 987−997

Table 1. Calculated Photophysical Properties of DABNA and its Related Molecules[a]

molecule	k_{RISC}[b] (10^4 s^{-1})	k_{SV} contribution (%)	ΔE_{ST}[c] (eV)	S_1[d] (eV)	SOC (cm^{-1})[e] S_1/T_1	SOC (cm^{-1})[e] S_1/T_3	NAC ($bohr^{-1}$)[f] T_1/T_3
DABNA	1.05	99.1	0.144 (0.15[g])	3.04 (2.71[g])	0.035	0.804	8.56
TBN-TPA	0.94	95.4	0.137 (0.14[h])	3.03 (2.64[h])	0.040	0.698	9.06
TABNA	0.16	99.9	0.161 (0.21[i])	3.36 (3.11[i])	0.005	0.439	14.23

[a]Experimental values in parentheses are from refs 8, 38, and 39. [b]Average rate in a small range around ΔE_{ST} as explained in the text. [c]Adiabatic singlet−triplet energy difference. [d]Vertical emission energy calculated at the S_1 geometry. [e]Triplet substate-averaged spin−orbit coupling. [f]Norm of the derivative coupling vector, $\|\langle T_3|\nabla|T_1\rangle\|$. [g]Measured in ethanol, [h]PMMA/1 wt % thin film, or in [i]toluene.

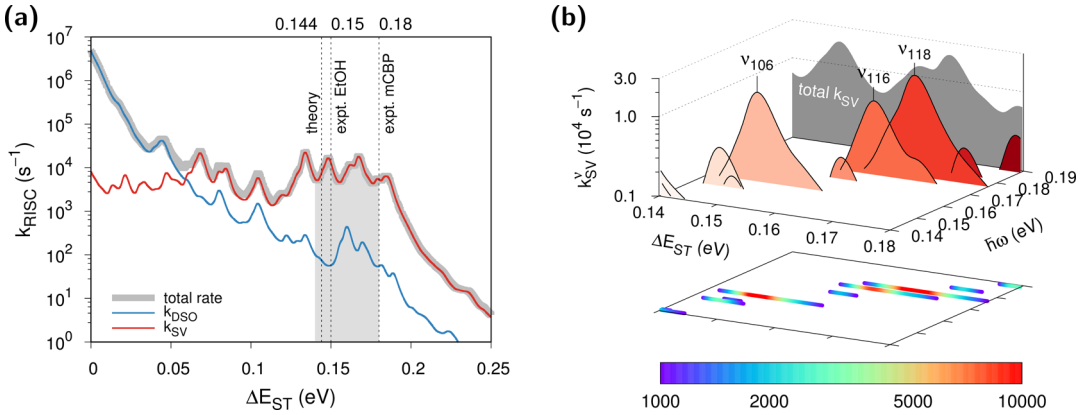

Figure 2. Vibronic enhancement of RISC. (a) Total RISC rate as a function of ΔE_{ST} and its decomposition into DSO and SV contributions. Some notable ΔE_{ST} values are marked as vertical lines: the computational (SCS-CC2) result at 0.144 eV; the experimentally observed gaps in ethanol solvent and in 3,3′-di(9H-carbazol-9-yl)-1,1′-biphenyl (mCBP) host at 0.15 and 0.18 eV. (b) Deconvolution of the SV component into each normal mode contribution in the ΔE_{ST} range of 0.14−0.18 eV. Rate contributions greater than 1000 s^{-1} are shown. The vertical scale is visually supplemented by the coloring scheme shown at the bottom. The contribution sum is depicted by the gray projection. The vibrational frequencies are represented along the axis denoted with $\hbar\omega$.

between excited states improves the quality of perturbation expansions.

We estimated the RISC upconversion kinetics with the golden rule formula, as it can provide a quantitative basis for understanding physical characteristics governed by thermally populated vibrational states of the initial T_1 state. Presuming an instantaneous thermalization among the substates of T_1 with $M = 0$ and ± 1, the rate constant of RISC is given by[24]

$$k_{RISC} = \frac{2\pi}{3\hbar}\sum_{M}\sum_{\nu\nu'} P_\nu(T)|H'_M|^2\delta(-\Delta E_{ST} + E_\nu - E_{\nu'}) \quad (1)$$

where the δ-function imposes energy conservation with the T_1 and the S_1 vibrational energies E_ν and $E_{\nu'}$. The thermal population at temperature T is described by Boltzmann distribution P_ν. The nonadiabatic interaction between the two electronic states is represented by $H'_M = \langle S_{1,\nu'}|\hat{H}'|T^M_{1,\nu}\rangle$ originating from the spin−orbit (SO) and the non-Born−Oppenheimer (nBO) couplings, $\hat{H}' = \hat{H}^{SO} + \hat{H}^{nBO}$. After perturbatively expanding both T_1 and S_1 state vectors with respect to $\hat{H}^{nBO}$ within their respective spin manifolds T′ and S′, one can show that the coupling matrix element can be expressed as a sum-over-state expansion:[25,26]

$$H'_M = H^{SO}_{S_1T_1} + \frac{1}{2}\sum_{T'} H^{SO}_{S_1T'}H^{nBO}_{T'T_1}\left(\frac{1}{E_{T'} - E_{T_1}} + \frac{1}{E_{T'} - E_{S_1}}\right) + \frac{1}{2}\sum_{S'} H^{nBO}_{S_1S'}H^{SO}_{S'T_1}\left(\frac{1}{E_{S'} - E_{T_1}} + \frac{1}{E_{S'} - E_{S_1}}\right) \quad (2)$$

The first term represents first-order direct spin−orbit (DSO) coupling driven by the electronic characters of S_1 and T_1, while the second and the third terms serve as second-order spin−vibronic (SV) coupling, where intermediary states in the triplet and the singlet manifolds assist the spin−orbit coupling. See also Supporting Information (SI) Text 1 for the derivation details on the coupling matrix elements of the full second-order SV terms.

The rate constant k_{RISC} can be analytically solved from a correlation function formalism combined with a path-integral expression[27−30] as briefly summarized in SI Text 1. Because k_{RISC} involves $|H'_M|^2$, it includes pure DSO and SV contributions from the squares of the corresponding terms in eq 2. We will respectively refer to them as k_{DSO} and k_{SV}. Of course, an SV−DSO cross term will also arise, but it vanishes due to time-reversal symmetry.[30] The calculated rate constants are listed in Table 1 together with other related photophysical properties obtained by quantum chemical calculations. One can see that our computed k_{RISC} of 1.05×10^4 s^{-1} agrees quite well with the experimental value of 0.99×10^4 s^{-1} measured in a thin film condition.[8] Of course, care must be taken in assessing the degree of agreement as both theory and experiment will surely have limitations when estimating rate constants.

Direct Spin−Orbit Coupling versus Second−Order Spin−Vibronic Coupling

In fact, what is much more important than observing a numerical agreement is analyzing the driving force for the spin crossover. The spin−orbit coupling between the T_1 and the S_1 states of DABNA is merely ~0.04 cm^{-1}, which is clearly insufficient to incur any meaningful RISC unless it is matched with an unphysically very small ΔE_{ST} (<0.05 eV). From Table 1, one can

https://doi.org/10.1021/jacsau.1c00179
JACS Au 2021, 1, 987−997

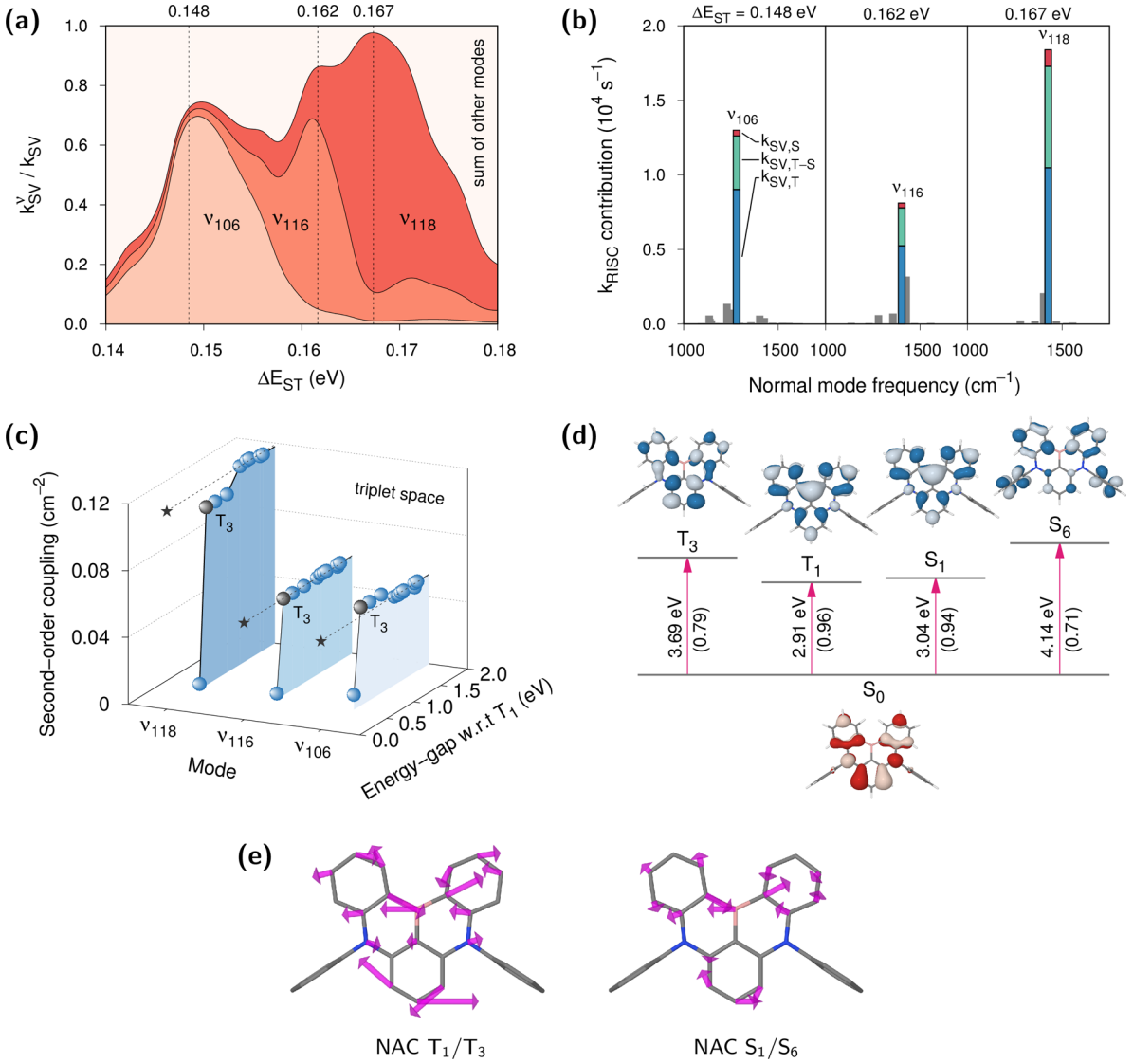

Figure 3. Analysis of k_{RISC} in DABNA. (a) Contributions by vibrational modes with strong resonance enhancements, namely ν_{106}, ν_{116}, and ν_{118}. The ΔE_{ST} values at which k_{SV}^{ν} become maxima are marked as vertical lines. (b) Contributions by each vibrational mode to k_{SV} at the vertically marked energies in a. The contribution is further partitioned into spin-manifold components according to eq 4. (c) Convergence profiles of the sum-over-electronic-states expansion for each mode in the triplet manifold. Similar profiles in the singlet manifold are provided in Figure S1. Here, the excited state with a dominant contribution (T_3) can be easily identified as marked with gray spheres. Convergence was reached with 20 excited states as denoted with dashed lines and stars. The T_1 energy was used as the zero energy reference. (d) Natural transition orbital pairs from the ω*B97X calculations at the S_1 geometry. Hole (red) and particle (blue) wave functions are represented by frontier orbitals with the largest weights, shown in parentheses. The S_1 and the T_1 energies are from the SCS-CC2 level calculations. (e) Nonadiabatic T_1-T_3 and S_1-S_6 coupling vectors responsible for RISC.

see that k_{SV} affected by intermediary spin states actually dominates k_{RISC}. To gain further insights, we parametrically varied ΔE_{ST} in the golden rule estimation and subsequently recalculated k_{RISC}. Figure 2a displays the RISC rate constants thus obtained. The single ΔE_{ST} value as obtained with the adopted SCS-CC2 method is marked with a vertical line, together with experimental ΔE_{ST} values measured under two different conditions.[8] Surprisingly, unlike typical organic molecules, the trend of the rate constants deviates substantially from the conventional energy gap law, which would manifest as a linearly decaying line in our log-scaled plot. Based on a deconvolution into k_{DSO} and k_{SV} portions also shown in Figure 2a, this unusual kinetic behavior can be attributed mainly to the latter spin−vibronic part.

Not only is RISC dynamics completely governed by SV coupling, but k_{SV} also remains nearly constant within an order of magnitude when ΔE_{ST} is in 0.14−0.18 eV. This range actually covers all ΔE_{ST} values predicted by both theory and experiment and was used for calculating average rates reported in Table 1. Beyond this range, k_{SV} decays in a monotonous manner following the energy gap law. We have further broken down the rate components associated with each vibrational normal mode as k_{SV}^{ν} (Figure 2b). We immediately see that, in this range, multiple modes can contribute quite significantly to enhancing the RISC rate in a successive and overlapping manner as long as their frequencies match ΔE_{ST} closely. For instance, if ΔE_{ST} is 0.148 eV (close to both theoretical and experimental values), the calculated total rate of 1.95×10^4 s^{-1} is mainly governed by a single vibrational mode "ν_{106}" at 1279 cm^{-1}. Without the SV

https://doi.org/10.1021/jacsau.1c00179
JACS Au 2021, 1, 987−997

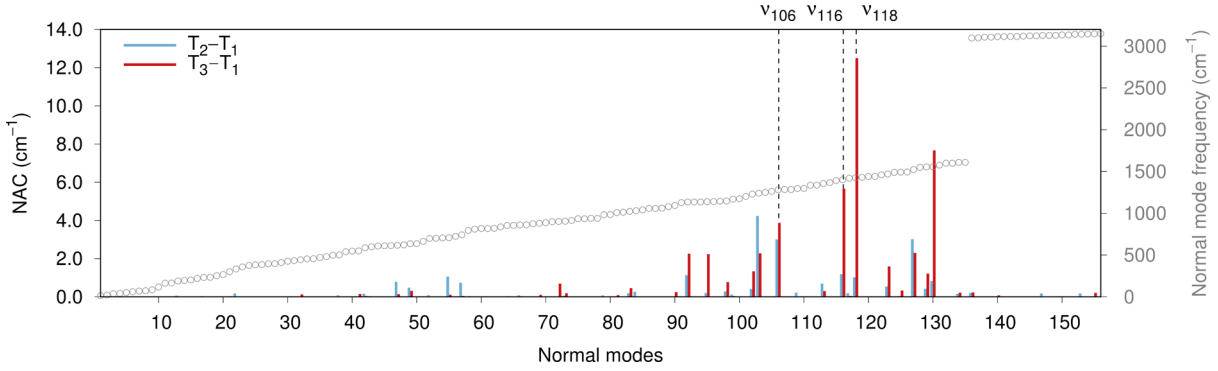

Figure 4. Mode−projected nonadiabatic couplings between T_2 and T_1 (blue) and between T_3 and T_1 (red). Projections were carried out onto each mode vector, normalized in the atomic unit ($\sqrt{m_e}$·bohr). Each mode is supplemented with its vibrational frequency (gray). Modes at 3000 cm^{-1} and above are stretches involving terminal hydrogen atoms.

contribution, k_{RISC} would have been as small as k_{DSO} = 56 s^{-1}. Similar analyses were also performed for other gaps and are shown in Table S1.

At first sight, as accelerations in exciton transfers by gap-matching vibrations have been continuously reported,[31−34] this RISC enhancement may appear trivial: spin crossover via a resonance between $S_{1,\nu'=0}$ and $T_{1,\nu=1}$. In the present case, however, T_1−S_1 SOC is very small, and k_{DSO} is still small even in the existence of a resonant vibration. Indeed, from Figure 2a, one can see that RISC by only DSO would have been 2 orders of magnitude slower even with the vibronic resonance. RISC becomes sufficiently fast only when the process is mediated by another electronic state, and the mediation is somehow strongly influenced by the vibrational frequency. Thus, we now turn our attention to which intermediary state plays the most important role in enhancing RISC rate in DABNA.

Contributions by Individual Electronic States

The successive vibronic enhancements by an array of vibrational modes serve to sustain the RISC rate for a plausibly expected range of ΔE_{ST} in DABNA. When we focus on three normal modes, ν_{106}, ν_{116}, and ν_{118}, which preeminently contribute to the total k_{RISC} as shown in Figure 3a, SV coupling through the triplet manifold originating from the second term in eq 2 is dominant as denoted by $k_{SV,T}$ in Figure 3b. On the other hand, the contribution from the singlet manifold, $k_{SV,S}$, is the least significant. Interestingly, the singlet manifold contributes more substantially via the cross-product of the second and the third terms, shown with $k_{SV,T-S}$ in Figure 3b. To identify important upper excited states that vibronically mediate T_1 and S_1, Figures 3c and S1 show the convergence profiles of the sum-over-states expansions in eq 2 again with respect to ν_{106}, ν_{116}, and ν_{118}. In the triplet manifold, which often acts as an important route toward spin−vibronic mixing, the nonadiabatic coupling effect between the T_1−T_3 pair is the most noticeable. For example, the nonadiabatic coupling between these states caused by a displacement corresponding to the normalized ν_{118} mode vector amounts to 12.5 cm^{-1} (Figure 4). This is enormously larger than the conventional SOC size in organic molecules. In addition, SOC between S_1 and T_3 is approximately 23 times larger than that between S_1 and T_1 (Table 1). This confirms that it is the T_3 state, which strongly mixes with the T_1 state via the "ΔE_{ST}-matching" vibrational mode, that enhances k_{SV}.

It is noteworthy that the T_2 state, on the other hand, even with a reduced energy gap, has relatively insignificant contribution to the total coupling due to little nonadiabatic component along the same ΔE_{ST}-matching vibrational mode. This might be surprising when one considers that the T_2−T_1 nBO coupling is slightly larger than the T_3−T_1 coupling at least along a few vibrational modes (Figure 4). At this point however, we emphasize that, from the perturbative expansion in eq 2, the total coupling responsible for RISC is determined by the product of nBO coupling and SOC terms between vibronic states. This combined coupling will undoubtedly be the decisive factor and revealing the important electronic state should be judged based on that combined factor. Given that T_2−S_1 SOC is only ∼1/3 of T_3−S_1 SOC (Figure S2), T_2 will not be able to outcompete T_3 with slight advantages that are only occasionally found in Figure 4. Namely, the combination of nBO coupling and SOC renders T_2 not as important toward promoting resonantly enhanced vibronic RISC. Even the mode ν_{103}, along which the T_2−T_1 coupling has the largest component in Figure 4, afforded at best 12.5% of the k_{RISC} at ΔE_{ST} = 0.146 eV, where the spin crossover was mostly steered by the T_3−T_1 coupling along the ν_{106} direction (Figure 3a).

To reason why the T_3−T_1 nBO coupling dominates, we may resort to the relationship between the spatial motions of three gap-matching vibrational modes and the nature of the electronic transitions. The atomic motions of the modes are in general along in-plane ring distortions (Figure S3) and will match well with the changes in conjugation patterns. The electronic change characterized by the switch from the T_1 particle wave function to the T_3 one shown in Figure 3d indeed shares a similar character. However, care must be taken with this reasoning. In the case of the T_2−T_1 pair, because the two states share almost the same particle wave functions (Figure S4), the electronic change may be characterized by the switch from the T_1 hole wave function to the T_2 one. In fact, this change is also with a conjugation switch. This aspect also cautions us against overusing the natural transition orbitals in reasoning for three-state-involving transition properties. As the nature of electronic transitions is determined by the involved many-electron wave functions, reasoning by visualizing one electron orbitals may become oversimplifications at times. Though computationally demanding, verifying with numerical data as presented here can form the clearest evidence.

The fact that T_2 contributes little is in line with an earlier report with MCTDH simulations,[15] where no appreciable T_2−T_1 internal conversions were found. In fact, if we had considered only T_1 and T_2 as in that report, we would have observed that the singlet manifold would contribute more than the triplet one by inferring from, for instance, a largish singlet coupling for ν_{118}

https://doi.org/10.1021/jacsau.1c00179
JACS Au 2021, 1, 987−997

(Figure S1) that is bigger than the T_2-coupling (Figure 3c). In addition, we believe that the cross-product term $k_{SV,T\text{-}S}$ is particularly enhanced because there is an electronic state that strongly resembles T_3 in the singlet manifold. Namely, the electronic character of S_6 is very similar (Figure 3d), and accordingly, the directionality of the nonadiabatic coupling vectors between the S_1−S_6 and the T_1−T_3 pairs will also be similar (Figure 3e). As a result, the second-order spin−vibronic transition paths between the T_1 and the S_1 states that involve the two intermediary states will likely cooperate.

Resonance Enhancement that Involves Three States

Now that we identified T_3 as the most important intermediary state for DABNA, we can infer that there is a strong and peculiar resonance enhancement in k_{SV} from a vibration (1) because it oscillates at a frequency that matches ΔE_{ST} and (2) because it induces strong T_1−T_3 coupling. This vibronic resonance is peculiar and is different from earlier observations[31−34] in that it involves more than two electronic states. We also stress that this superexchange process involving T_3 should be distinguished from a stepwise conversion including the "reverse internal conversion" (RIC) from T_1 to T_3. The calculated gap between the two electronic states is much larger than the thermal energy with $\Delta E_{T_3T_1} \sim 30k_BT$ (Table S2), and as a result the equilibrium constant between T_1 and T_3 will be diminutive. Furthermore, S_1 and T_3 are not isoenergetic with $\Delta E_{T_3S_1} \sim 4\Delta E_{ST}$, which will also significantly prohibit the spin conversion between these states. Should the RISC process take place via the spin crossover as $T_3 \rightarrow S_1$ after a pre-equilibrium involving RIC as $T_1 \rightleftharpoons T_3$, the overall rate will be too slow. One may also wonder about the role of T_3 hot excitons that can form transiently during electroluminescence. For DABNA, a direct hot exciton transfer from T_3 to S_1 is appraised as an unlikely event, because with the strong vibronic coupling between the two triplets, the $T_3 \rightarrow T_1$ transition will prevail and lead to an almost complete and instant population transfer to the lowest triplet.

To further substantiate the peculiar resonance, we have also employed a semiclassical quantum dynamics simulation approach, Poisson bracket mapping equation (PBME-nH).[35,36] Based on the observations described in the above, we have chosen $\{S_1, T_1, T_3\}$ as our electronic state space. These states and one underdamped vibration corresponding to ν_{106} form our minimal model for exhibiting the resonance. The underdamped mode actually vibronically couples T_1 and T_3, and the coupling strength changes in proportion to the normal mode displacement (see Computational Methods). To further probe the resonant behavior by ν_{106}, we scanned its frequency around its physical value. Figure 5 displays how k_{RISC} changes as a function of this frequency and we can indeed directly observe a resonant behavior again near the physical frequency, 1279 cm^{-1} (= 0.159 eV). As is shown in the same figure, when we fortuitously set the T_1−T_3 coupling as constant in time with the ν_{106} mode still preserved in the system, the S_1 population did not grow any faster than what was allowed by the small SOC between T_1 and S_1, even when the constant T_1−T_3 coupling was rather strong and the ν_{106} frequency matched ΔE_{ST}. Thus, the fluctuating nature of the T_1−T_3 coupling is the key to the RISC enhancement, which is maximized when the fluctuating frequency is in a near-resonant condition with ΔE_{ST}.

It is intriguing to observe that the vibrational resonance involves three electronic states, with the frequency matching both the energy gap for the T_1−S_1 pair and the coupling oscillation for the T_1−T_3 pair. Thus, RISC enhancement

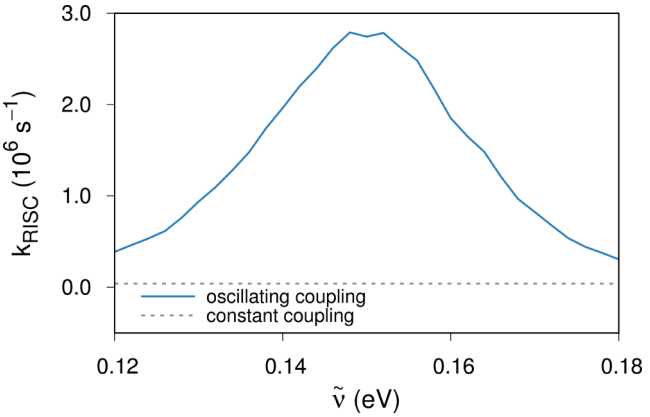

Figure 5. Resonance enhancement of RISC by a coupled vibration. The blue line denotes the rate estimated with PBME-nH quantum dynamics simulations with an underdamped emitter vibration with a frequency $\tilde{\nu}$ that induces T_1−T_3 coupling in a non-Condon manner. The gray line shows the rate with a strong constant coupling but without this non-Condon effect, $V_{T_1T_3}$ = 500 cm^{-1}.

through SV coupling bears a strong superexchange character.[37] When this peculiar resonance condition is met, the RISC process can take place even when ΔE_{ST} is rather substantial as was already noted with Figure 2a. This interesting behavior can be explained in the following manner. The oscillating non-Condon T_1−T_3 coupling ($V_{T_1T_3}$) forces the electronic characters of a triplet state to alternate in time. Namely, a state initially at T_1 will become a superposition of T_1 and T_3, whose composition will vary with the vibrational motion. Because the T_3−S_1 SOC is relatively large (Table 1), the new superposition state can transfer the population to S_1 with a much larger probability than the pure T_1. In addition, because $V_{T_1T_3}$ oscillates in time, the T_3 composition will keep fluctuating and sustain the transfer until all triplet population is consumed. Surprisingly, if $V_{T_1T_3}$ is constant in time, i.e., Condon coupling, the electronic character of the triplet state quickly settles to a steady state, from which the RISC process is not as effective. In fact, the constant coupling adopted with Figure 5 was twice larger than the root-mean-squared average of the oscillating coupling. The fact that the two RISC kinetics shown in the figure are drastically different evidently exhibits the importance of the oscillating nature of the vibronic coupling, with the matching resonance condition with ΔE_{ST}. Perhaps, the resonantly fluctuating coupling is taking a role of replenishing the fragile coherence[31] between T_1 and T_3. We note that the time scale of state transitions in OLED materials is often much longer than that of light harvesting systems, and it is striking that there can still be a process with commonly shared characters[31] between the two different groups.

The physical foundation of the spin−vibronically enhanced RISC at substantial ΔE_{ST} can be additionally explained with Figure 6a, where molecular factors affecting k_{SV} are schematically displayed. Because both the S_1 and the T_1 states share the identical local excitation character, the potential energy surfaces are quite similar in shape to each other. In addition, structural rigidity stemming from extensive conjugation in combination with planarity resembling nanographene restricts the T_1−S_1 geometric distortion as $\vec{d} \sim 0$ (Figure S5). These aspects combine to produce only slightly shifted vibrational frequencies and a diagonal-dominant Duschinsky matrix from T_1 to S_1

https://doi.org/10.1021/jacsau.1c00179
JACS Au 2021, 1, 987−997

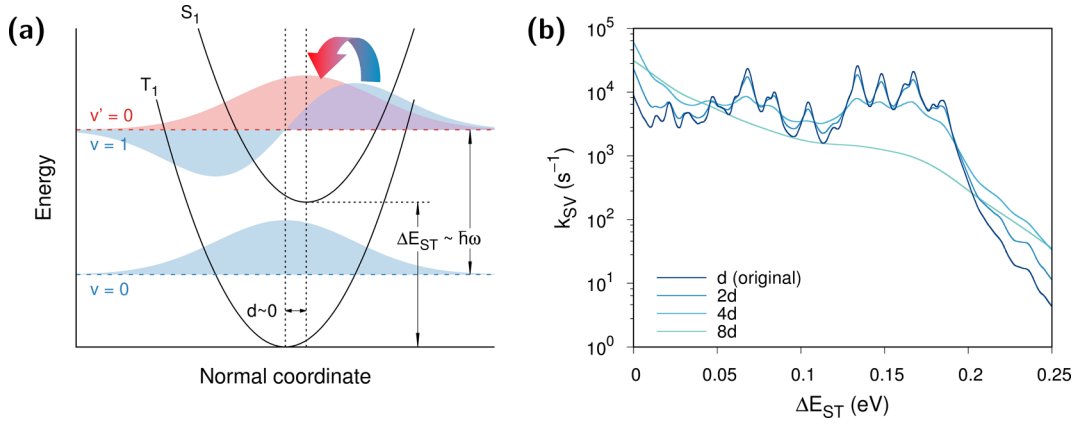

Figure 6. Mechanism of vibrational enhancement of RISC. (a) Schematic representation of the vibronic spin-flip transition. The vibrational wave functions are illustrated with filled curves (T_1, blue; S_1, red). (b) Displacement dependence of the second-order (spin−vibronic) RISC rates at varying ΔE_{ST} as measured by fortuitously increasing the original displacement vector $\vec{d}$ by some integers, $\vec{d}' = 2n\vec{d}$. See SI Text 1 for the mathematical formulation of $\vec{d}$.

(Figure S6), resulting in no normal mode mixing upon state switching. RISC dynamics can therefore be reduced to independent mode-by-mode dynamics (Figure 6a). When $\Delta E_{ST} \neq 0$, the δ-function in eq 1 and hence k_{RISC} will reach a maximum as ΔE_{ST} approaches the vibrational gap $\hbar\omega$. In addition, as discussed above, the spin crossover process is undertaken through the state mixing with T_3 especially when $\vec{d}$ is along the T_1-T_3 coupling direction. Therefore, for an optimal k_{RISC}, $\vec{d}$ along ν_{106} must remain small to maximize the Franck−Condon factor and the derivative integral between the $\nu = 0$ and the $\nu' = 1$ vibrational wave functions (SI Text 1). The effect of the displacement can be easily verified numerically by increasing the quantum chemically obtained $\vec{d}$ into fortuitously larger $\vec{d}'$. Indeed, the vibronic enhancement in k_{SV} almost disappears at large $\vec{d}'$ in the golden rule rate estimation (Figure 6b), and a similar behavior is also observed from PBME-nH simulations (Figure S7). We also note that at larger ΔE_{ST}, increasing $\vec{d}$ will lead to a slower decay of k_{DSO} (Figure S8). The temperature effect was also investigated (Figure S9), affirming that k_{SV} becomes more prominent at higher temperature because the transition originates from a thermal population at $\nu = 1$.

Behaviors of DABNA Variants

We further applied the same golden-rule rate analysis to a few more emitting molecules related to DABNA (Table 1 and Figure S5). First, TBN-TPA with a carbazole group in a *para*-position to boron and six additional *tert*-butyl groups on peripheral phenyl rings was investigated. As shown in the table, the added carbazole moiety only slightly reduces ΔE_{ST} by ∼0.01 eV. At this energy gap, predominance of the SV contribution was retained (Figure S10a). If we assume that we can tune the energy gap by changing the doping conditions, our calculations indicate that it will be possible to obtain a maximum k_{RISC} at 1.07×10^4 s^{-1} appearing at $\Delta E_{ST} \simeq 0.15$ eV. The average rate over a small range (±0.1 eV) of ΔE_{ST} is estimated as 0.94×10^4 s^{-1}. This is comparable to DABNA, allowing us to speculate that the reported higher PLQY (98%) from an earlier experiment[38] is due to the bulky *tert*-butyl groups that physically hinder external quenching factors. TABNA with an added phenylamino group onto the DABNA core was also considered, even though its emission is excessively blue-shifted with $\lambda_{max} = 399$ nm.[39] In this case, while k_{SV} still governed the RISC dynamics because T_1-S_1 SOC was almost negligible, the absolute value of k_{SV} was smaller by an order of magnitude, resulting in no vibrational resonance peaks (Figure S10b). This is mainly due to a much larger geometric difference between T_1 and S_1 states, corresponding to a reorganization energy of $\lambda = 434$ cm^{-1} by the emitter itself. This reaffirms that a small geometric change is needed to observe vibrational enhancement of k_{SV} (Figure 6).

Finally, we note that the energy gap between the vibronically coupled triplet pair (the T_1-T_3 gap for DABNA) will also be important for efficient and practical RISC. This is easily discernible both with the golden rule and PBME formalisms. When the gap is too large, the contribution of T_3 in the perturbation expansion for T_1 diminishes. Likewise, T_1-T_3 mixing in PBME weakens under the same condition and the effect of superexchange becomes unimportant. Therefore, reducing this gap should also be a tactic of consideration if one attempts to optimize k_{RISC} through k_{SV}. Of course, achieving this without disturbing electronic structure properties, such as the MR effect, will be important, as breaking it can return the emitter properties to conventional DA-type behaviors.[40] Indeed, we have already seen that TABNA does not exhibit a resonantly enhanced RISC rate even with the reduced T_1-T_3 gap (Table S3) and subsequently increased nonadiabatic coupling (Table 1). This is because the electronic structure consistency between S_1 and T_1 is broken with the added modification from DABNA.

Donor−Acceptor Type versus Multiple−Resonance Type Emitters

Due to conflicting preferences for the exchange energy K,[41] DA-emitters tend to have different natures in their lowest excited states: charge-transfer (CT) S_1 vs locally excited (LE) T_1 states.[42,43] This entails relatively large geometric differences (Table S4) and, subsequently, large reorganization energies during ISC between them. While a small displacement can be expected for DA type emitters when both the S_1 and the T_1 states correspond to the same CT character, the displacement will likely be still larger than in DABNA. This is because there should be another LE triplet state whose energy is close to the T_1 energy to facilitate the RISC process. With the neighboring LE state, due to inevitable electronic mixing, T_1 will still have a non-negligible amount of LE character, which will subsequently induce a noticeable size of displacement from the S_1 geometry. As we observed in Figure 6b, the vibrational rate enhancement in

https://doi.org/10.1021/jacsau.1c00179
JACS Au 2021, 1, 987−997

k_{SV} disappears when $\vec{d}' = 8\vec{d}$. The reorganization energy of $8\vec{d}$ amounts to 2128 cm^{-1} ($\equiv\sum_\nu \frac{1}{2}d'^2_\nu\omega^2_\nu$), which is close to the reorganization energies of DA-TADF emitters. Thus, it explains why a drastic vibrational enhancement in k_{SV} was not observed in more flexible DA-TADF emitters in an earlier study.[30] In addition, El-Sayed-allowed DSO between a charge transfer S_1 state and a locally excited T_1 state provides the primary pathway to RISC, with reducing ΔE_{ST} working as the widely accepted design principle.[4,42,43] Hence, for DA-TADF emitters, the DSO portion will play a major role with a minor enhancement from SV coupling.[30] We should, however, note that by exploiting the disparate responses of CT and LE states to the surrounding polarity, the ^{1}CT−^{3}CT pair can be (quasi-)degenerate or be even more stable than the ^{3}LE state in a polar medium. In such cases, the SV coupling can be elevated for DA-TADF emitters at the expense of a redshift in the emission wavelength.[13]

Owing to the similarity between the electronic structures of T_1 and S_1, ΔE_{ST} of DABNA, *albeit* being reduced by electron correlations, remains relatively large. In addition, the DSO coupling between T_1 and S_1 is suppressed by the El-Sayed rule.[44] However, such an electronic structure similarity gives rise to a small geometric displacement in the spin crossover. If there is a vibrational mode that energetically matches ΔE_{ST} and effectively induces the coupling between the lowest excited state and higher-lying intermediary state, then such a SV coupling can speed up the RISC process dramatically. It is evident that, from the existence of multiple modes with such properties, the vibronic enhancement can be contiguous over extended ΔE_{ST} values. These aspects will defy the energy gap law that essentially governs the RISC processes in DA-TADF molecules.

With the above comparisons, it will be interesting to further consider how the present case differs from the recently discussed spin−vibronic mechanism with a third mediating state in a DA-TADF system DPTZ-DPTO2.[13,14] As a matter of fact, the spin−vibronic mechanism of state switching involving two different spin multiplicities has been known for quite some time (for instance, ref 25), and there can be many different possibilities through which the mechanism can manifest itself. In the case of DPTZ-DPTO2, the energy resonance condition between the involved electronic states was discussed to be crucial, and the "Type II" case with ^{1}CT, ^{3}CT, and ^{3}LE states gathered together at near-degeneracy was suggested as an ideal system for TADF. When that condition is met, because the spin−orbit coupling is much larger for the ^{3}LE−^{1}CT pair than for ^{3}CT−^{1}CT, and because ^{3}LE is thermally quite accessible, RISC via ^{3}LE−^{1}CT will play a dominant role either through a direct transfer or through mediation involving ^{3}CT. In this case, a vibration plays only a nonadiabatic coupling role for the ^{3}LE−^{3}CT pair but not for the energy resonance. Our results with the MR-TADF system, whose $S_1/T_1/T_3$ states play the somewhat analogous roles of ^{1}CT/^{3}CT/^{3}LE of the DA-TADF system, show different behaviors in a few crucial ways.

1. The T_1 energy is noticeably lower than the S_1 energy in MR-TADF. Thus, a vibration should be combined to satisfy the energy resonance condition to facilitate the T_1−S_1 conversion. Indeed, we have verified the associated RISC rate enhancement as shown in Figures 2 and 5. Again, the vibrational frequency resonance is a key to MR-TADF but not for DA-TADF. Also, there are multiple vibrations that can resonantly enhance the state switching rate.
2. The mediating T_3 state in DABNA is quite high in energy and is thermally inaccessible for hopping or reverse internal conversion. On the other hand, in DA-TADF systems, the mediating ^{3}LE state tends to lie below the ^{3}CT level especially when ΔE_{ST} is large and a significant spin−vibronic effect is expected. This difference induces many different aspects: for example, the extraordinarily large non-Condon effect, which appears important for the RISC rate enhancement with DABNA.
3. The geometric distortion associated with the $T_1 \rightarrow S_1$ switch is quite small with DABNA, whereas the equivalent distortion with a DA-TADF molecule tends to be large when T_1 is ^{3}LE, with different characters from ^{1}CT as S_1 (Table S4). Indeed, we found that a large distortion will simply erase the resonant vibronic RISC enhancement (Figure 6b), and the vibrational rate enhancement as in DABNA will not be observed in DA-TADF systems.

This leads us to an important alternative of designing effective MR-TADF emitters: the optimal SV coupling through vibronic resonance. For certain molecules like DABNA, lowering ΔE_{ST} can often be challenging. Sometimes, peripheral substitutions for improving other functionalities such as intermolecular interactions and charge transport behaviors should often be conducted even at the cost of increasing ΔE_{ST}. In such cases, it will be ideal if the increase in ΔE_{ST} can be compensated by the vibrational resonance effect. One may be concerned that the resonance would be too fragile as the gap energy can be easily changed by the emitter environment and matching the frequency might be too restrictive. We believe this will not be too serious as there may be multiple vibrations that can play the enhancing role. With DABNA, indeed, three modes with enough overlaps with the T_1−T_3 derivative coupling (Figure S3) can take their turns when ΔE_{ST} was varied (Figure 2). In addition, the resonance peaks are actually quite broad (Figures 2 and 5), and strictly matching the frequency is not a necessity.[34]

CONCLUSION

We have applied a spin−vibronic model and a semiclassical quantum dynamics simulation tool to elucidate the RISC dynamics of MR-TADF organoboron emitters with superior color purity. We found that it is highly driven by a spin−vibronic effect, which emerges as a second-order process with the golden rule description and as a superexchange event from the semiclassical treatment. More importantly, we observed a peculiar three-state involving resonance with which the RISC rate is enhanced significantly when the frequency of a vibration that induces a non-Born−Oppenheimer coupling between the T_1−T_3 pair matches the gap energy between the T_1−S_1 pair. We also showed that multiple vibrational modes exist so that they can resonantly enhance exciton transfers over a wide enough range of ΔE_{ST}.

The fact that the spin−vibronic effect plays a major role in the considered MR-TADF emitters is in stark contrast to the aspect observed with more conventional DA-TADF emitters, where the dynamics could be explained largely by the first-order direct spin−orbit coupling.[30] Perhaps, the widely accepted design principle for achieving superior TADF emitters by minimizing ΔE_{ST} may not be the only path to consider at least for the emitters with rigid core structures, and maximizing the spin−vibronic coupling through vibronic resonance can be additionally sought for. Nonetheless, predicting in an *a priori* fashion whether a vibration will participate to resonantly enhance RISC

https://doi.org/10.1021/jacsau.1c00179
JACS Au 2021, 1, 987−997

will not be a simple task as it requires comprehensively computing the emitter properties with the rather complicated network of excited states, as attempted in our present work. Even still, we conclude that treating spin−vibronic coupling is of utmost importance and should be included in a regular basis, as well-defined design principles based on second-order effects will surely benefit the development of efficient emitters. As is often the case with any excited state tuning, predicting the relationships between multiple modification aspects will be a complicated undertaking, but a viable solution can still be reached by adopting advanced tools as screening measures. We hope that our approaches described here can serve such a purpose in future molecular designs.

COMPUTATIONAL METHODS

Electronic Structure Calculations

Electronic structure calculations were performed with the TURBOMOLE 7.3[45] and Q-Chem 5.1[46] program packages. With the original spin-component scaling parameters,[47] the excited state geometries were optimized by the strict variant of the second-order algebraic diagrammatic construction (SCS-ADC(2)) method.[48] This was followed by the approximate coupled-cluster singles and doubles (SCS-CC2) method[49] for the energy evaluations. The resolution-of-the-identity approximation for the electron repulsion integrals were used in treating correlations. For normal mode calculations, numerical Hessians were employed with a frequency scaling factor of 0.9631.[50] The optimized geometries and the corresponding vibrational frequencies are provided in Tables S5 and S6. Because the nonadiabatic and spin−orbit couplings were not available at the ADC(2) or CC2 level, single-point time-dependent DFT calculations under the Tamm−Dancoff approximation was adopted instead, with the gap-tuned long-range corrected ω*B97X functional.[51] Because the nuclear screening two-electron term is often small and is less important in the context of spin−vibronic model with the more contributing vibronic coupling, we have employed the one-electron Breit−Pauli spin−orbit Hamiltonian.[52] Solvent effects were treated with the polarizable continuum model in the integral equation formalism (IEF-PCM).[53] The amorphous molecular solid film condition was imitated by the parameters of $\epsilon = 2.84$ and $n = 1.7$, derived from an archetypal blue host material 1,3-bis(*N*-carbazolyl)benzene (mCP). Natural transition orbital (NTO) analyses were postprocessed by TheoDORE 2.0 package.[54] The def2-SVP basis set was used for all calculations. A number of progressively larger basis sets were tested in order to evaluate the basis set effect on ΔE_{ST} and only slight shifts were observed. See SI Text 2 for other details.

Golden Rule Rates

Fermi's golden rule rate calculations with the time-correlation function formalism[30] were carried out through the discrete Fourier transform with the FFTW 3.3.6 library.[55] The time integration was performed in the domain of [−6553.6:6553.6] fs and the time correlation functions were discretized in steps of 12.5 ps, which corresponded to 2^{19} points in the positive time direction. Of course, the rate expression is obtained with the square modulus of eq 2. Because the rate in eq 1 includes infinity from the δ-function, damping is often introduced to avoid divergence in k_{RISC}.[56,57] Physically, the damping time scale is related to the dephasing time of the involved excited state and is often difficult to deduce, which leads to a certain degree of ambiguity in the calculated rate. In our case with DABNA, there was no ambiguity because the rate change was quite insignificant for any damping time chosen in a wide range of 1 ps $\leq \gamma \leq$ 100 ns. See SI Text 3 for more details.

Because the cross-product of the DSO and the SV terms vanishes due to the time-reversal symmetry,[30] the total RISC rate can be neatly partitioned into individual components:

$$k_{RISC} = k_{DSO} + k_{SV} \quad (3)$$

Because there are two SV terms in eq 2, the spin cross-product from the second and the third terms in that equation does not vanish and contributes to k_{SV}. Still, we can separately compare and contrast the contributions by the spin manifolds to gain insights into the details of the process:

$$k_{SV} = k_{SV,T} + k_{SV,S} + k_{SV,T-S} \quad (4)$$

as displayed in Figure 3b. This decomposition is feasible because, in the nonrelativistic regime, the singlet and the triplet excited states are computed independently from each other.

PBME-nH Simulations

The electronic subsystem Hamiltonian was defined by the two gap energies ($\Delta E_{S_1T_1} = \Delta E_{ST}$ and $\Delta E_{S_1T_3}$) and two SOC elements ($V^{SOC}_{S_1T_1}$ and $V^{SOC}_{S_1T_3}$). One harmonic underdamped mode (ν_{106}) was set to induce the nonadiabatic coupling between T_1 and T_3. Parameters for forming this Hamiltonian elements were taken from the quantum chemical data as listed in Tables 1, S3, S6, and S7. As the nonadiabatic coupling is dictated by the derivative coupling $\langle T_1|\nabla|T_3\rangle$ and fluctuates with geometric distortions by the ν_{106} normal mode motion, it is intrinsically non-Condon. The diagonal energy coupling by the normal vibrations of the emitter were included by considering the mode-specific reorganization energies as specified in Table S8. A thermal bath representing the emitter environment was also added as a Debye spectral density with a reorganization energy $\lambda_{ph} = 20$ cm^{-1}. Starting with 100% population at T_1 initially, multiple trajectory simulations were performed for 1 ps durations and k_{RISC} was obtained by monitoring the S_1 population growth in an extrapolating manner. More details about the quantum dynamics simulations can be found in SI Text 4.

ASSOCIATED CONTENT

Supporting Information

The Supporting Information is available free of charge at https://pubs.acs.org/doi/10.1021/jacsau.1c00179.

> Details about the adopted computational methods and the proof of the finiteness of k_{RISC}; Tables with normal mode specific analyses, quantum chemical data, S_1-T_1 geometric differences of MR and DA type emitters, and k_{RISC} dependence on the damping time parameter; Figures analyzing various nonadiabatic coupling, spin−crossover rates, and the related data based on normal modes and natural transition orbitals (PDF)

AUTHOR INFORMATION

Corresponding Authors

Won-Joon Son − *Data and Information Technology Center, Samsung Electronics, Hwaseong 18448, Republic of Korea;* orcid.org/0000-0003-4087-4661; Email: wonjoon.son@samsung.com

Dongwook Kim − *Department of Chemistry, Kyonggi University, Suwon 16227, Republic of Korea;* orcid.org/0000-0003-2096-3720; Email: dongwook-kim@kyonggi.ac.kr

Young Min Rhee − *Department of Chemistry, Korea Advanced Institute of Science and Technology (KAIST), Daejeon 34141, Republic of Korea;* orcid.org/0000-0002-2392-3962; Email: ymrhee@kaist.ac.kr

Authors

Inkoo Kim − *Data and Information Technology Center, Samsung Electronics, Hwaseong 18448, Republic of Korea;* orcid.org/0000-0002-1653-0992

Kwang Hyun Cho − *Department of Chemistry, Korea Advanced Institute of Science and Technology (KAIST),*

https://doi.org/10.1021/jacsau.1c00179
JACS Au 2021, 1, 987−997

Daejeon 34141, Republic of Korea; orcid.org/0000-0003-1316-3063

Soon Ok Jeon − *Samsung Advanced Institute of Technology, Samsung Electronics, Suwon 16678, Republic of Korea*

Inkook Jang − *Data and Information Technology Center, Samsung Electronics, Hwaseong 18448, Republic of Korea*

Hyeonho Choi − *Samsung Advanced Institute of Technology, Samsung Electronics, Suwon 16678, Republic of Korea;* orcid.org/0000-0002-6884-8193

Dae Sin Kim − *Data and Information Technology Center, Samsung Electronics, Hwaseong 18448, Republic of Korea*

Complete contact information is available at: https://pubs.acs.org/10.1021/jacsau.1c00179

Notes

The authors declare no competing financial interest.

■ ACKNOWLEDGMENTS

The authors thank Prof. Yoon Sup Lee (KAIST) for helpful discussions. D.K. and Y.M.R. acknowledge Samsung Electronics Co. Ltd. for financial support (IO 190115-05888-01). D.K.'s contribution was additionally supported by the Basic Science Research Program through the National Research Foundation of Korea (NRF) funded by the Ministry of Science and ICT (MSIT) of the Korea government (No. 2018R1D1A1A09084233). Y.M.R. is grateful for the support from another NRF grant funded by MSIT (No. 2020R1A5A1019141). Computational resources were provided by the Supercomputing Center of Samsung Electronics and by KAIST.

■ REFERENCES

(1) Uoyama, H.; Goushi, K.; Shizu, K.; Nomura, H.; Adachi, C. Highly efficient organic light-emitting diodes from delayed fluorescence. *Nature* **2012**, *492*, 234−238.

(2) Hirata, S.; Sakai, Y.; Masui, K.; Tanaka, H.; Lee, S. Y.; Nomura, H.; Nakamura, N.; Yasumatsu, M.; Nakanotani, H.; Zhang, Q.; Shizu, K.; Miyazaki, H.; Adachi, C. Highly efficient blue electroluminescence based on thermally activated delayed fluorescence. *Nat. Mater.* **2015**, *14*, 330−336.

(3) Wong, M. Y.; Zysman-Colman, E. Purely Organic Thermally Activated Delayed Fluorescence Materials for Organic Light-Emitting Diodes. *Adv. Mater.* **2017**, *29*, 1605444.

(4) Chen, X. K.; Kim, D.; Brédas, J. L. Thermally Activated Delayed Fluorescence (TADF) Path toward Efficient Electroluminescence in Purely Organic Materials: Molecular Level Insight. *Acc. Chem. Res.* **2018**, *51*, 2215−2224.

(5) Kaji, H.; Suzuki, H.; Fukushima, T.; Shizu, K.; Suzuki, K.; Kubo, S.; Komino, T.; Oiwa, H.; Suzuki, F.; Wakamiya, A.; Murata, Y.; Adachi, C. Purely organic electroluminescent material realizing 100% conversion from electricity to light. *Nat. Commun.* **2015**, *6*, 8476.

(6) Yang, Z.; Mao, Z.; Xie, Z.; Zhang, Y.; Liu, S.; Zhao, J.; Xu, J.; Chi, Z.; Aldred, M. P. Recent advances in organic thermally activated delayed fluorescence materials. *Chem. Soc. Rev.* **2017**, *46*, 915−1016.

(7) *Light Spectra for the Samsung Galaxy S10*, released in March 2019; http://www.displaymate.com/Spectra_47S.html (accessed 2021/04/26).

(8) Hatakeyama, T.; Shiren, K.; Nakajima, K.; Nomura, S.; Nakatsuka, S.; Kinoshita, K.; Ni, J.; Ono, Y.; Ikuta, T. Ultrapure Blue Thermally Activated Delayed Fluorescence Molecules: Efficient HOMO-LUMO Separation by the Multiple Resonance Effect. *Adv. Mater.* **2016**, *28*, 2777−2781.

(9) Kondo, Y.; Yoshiura, K.; Kitera, S.; Nishi, H.; Oda, S.; Gotoh, H.; Sasada, Y.; Yanai, M.; Hatakeyama, T. Narrowband deep-blue organic light-emitting diode featuring an organoboron-based emitter. *Nat. Photonics* **2019**, *13*, 678−682.

(10) Mellerup, S. K.; Wang, S. Boron-Doped Molecules for Optoelectronics. *Trends Chem.* **2019**, *1*, 77−89.

(11) Jiang, H.; Cao, Y.; Yang, Q.; Xian, L.; Tao, Y.; Chen, R.; Huang, W. Organic Resonance Materials: Molecular Design, Photophysical Properties, and Optoelectronic Applications. *J. Phys. Chem. Lett.* **2020**, *11*, 7739−7754.

(12) Vázquez, R. J.; Yun, J. H.; Muthike, A. K.; Howell, M.; Kim, H.; Madu, I. K.; Kim, T.; Zimmerman, P.; Lee, J. Y.; III, T. G. New Direct Approach for Determining the Reverse Intersystem Crossing Rate in Organic Thermally Activated Delayed Fluorescent (TADF) Emitters. *J. Am. Chem. Soc.* **2020**, *142*, 8074−8079.

(13) Etherington, M. K.; Gibson, J.; Higginbotham, H. F.; Penfold, T. J.; Monkman, A. P. Revealing the spin-vibronic coupling mechanism of thermally activated delayed fluorescence. *Nat. Commun.* **2016**, *7*, 13680.

(14) Gibson, J.; Monkman, A. P.; Penfold, T. J. The Importance of Vibronic Coupling for Efficient Reverse Intersystem Crossing in Thermally Activated Delayed Fluorescence Molecules. *ChemPhysChem* **2016**, *17*, 2956−2961.

(15) Northey, T.; Penfold, T. J. The intersystem crossing mechanism of an ultrapure blue organoboron emitter. *Org. Electron.* **2018**, *59*, 45−48.

(16) Penfold, T. J.; Gindensperger, E.; Daniel, C.; Marian, C. M. Spin-Vibronic Mechanism for Intersystem Crossing. *Chem. Rev.* **2018**, *118*, 6975−7025.

(17) Marian, C. M. Understanding and Controlling Intersystem Crossing in Molecules. *Annu. Rev. Phys. Chem.* **2021**, *72*, 617−640.

(18) Lin, L.; Fan, J.; Cai, L.; Wang, C. K. Excited state dynamics of new-type thermally activated delayed fluorescence emitters: theoretical view of light-emitting mechanism. *Mol. Phys.* **2018**, *116*, 19−28.

(19) Pershin, A.; Hall, D.; Lemaur, V.; Sancho-Garcia, J. C.; Muccioli, L.; Zysman-Colman, E.; Beljonne, D.; Olivier, Y. Highly emissive excitons with reduced exchange energy in thermally activated delayed fluorescent molecules. *Nat. Commun.* **2019**, *10*, 597.

(20) Kim, D. A theoretical understanding of the energy difference between singlet and triplet states of oligoacene molecules. *Int. J. Quantum Chem.* **2016**, *116*, 651−655.

(21) De Silva, P. Inverted Singlet-Triplet Gaps and Their Relevance to Thermally Activated Delayed Fluorescence. *J. Phys. Chem. Lett.* **2019**, *10*, 5674−5679.

(22) Tajti, A.; Szalay, P. G. Accuracy of spin-component-scaled CC2 excitation energies and potential energy surfaces. *J. Chem. Theory Comput.* **2019**, *15*, 5523−5531.

(23) Reimers, J. R. A practical method for the use of curvilinear coordinates in calculations of normal-mode-projected displacements and Duschinsky rotation matrices for large molecules. *J. Chem. Phys.* **2001**, *115*, 9103−9109.

(24) Peng, Q.; Fan, D.; Duan, R.; Yi, Y.; Niu, Y.; Wang, D.; Shuai, Z. Theoretical Study of Conversion and Decay Processes of Excited Triplet and Singlet States in a Thermally Activated Delayed Fluorescence Molecule. *J. Phys. Chem. C* **2017**, *121*, 13448−13456.

(25) Henry, B. R.; Siebrand, W. Between singlet and triplet states in benzene and naphthalene. *J. Chem. Phys.* **1971**, *54*, 1072−1085.

(26) Parker, S. M.; Shiozaki, T. Quasi-diabatic states from active space decomposition. *J. Chem. Theory Comput.* **2014**, *10*, 3738−3744.

(27) Peng, Q.; Niu, Y.; Shi, Q.; Gao, X.; Shuai, Z. Correlation function formalism for triplet excited state decay: Combined spin-orbit and nonadiabatic couplings. *J. Chem. Theory Comput.* **2013**, *9*, 1132−1143.

(28) Baiardi, A.; Bloino, J.; Barone, V. General time dependent approach to vibronic spectroscopy including Franck-Condon, Herzberg-Teller, and Duschinsky effects. *J. Chem. Theory Comput.* **2013**, *9*, 4097−4115.

(29) De Souza, B.; Farias, G.; Neese, F.; Izsák, R. Predicting Phosphorescence Rates of Light Organic Molecules Using Time-Dependent Density Functional Theory and the Path Integral Approach to Dynamics. *J. Chem. Theory Comput.* **2019**, *15*, 1896−1904.

(30) Kim, I.; Jeon, S. O.; Jeong, D.; Choi, H.; Son, W. J.; Kim, D.; Rhee, Y. M.; Lee, H. S. Spin-Vibronic Model for Quantitative Prediction of Reverse Intersystem Crossing Rate in Thermally Activated Delayed Fluorescence Systems. *J. Chem. Theory Comput.* **2020**, *16*, 621−632.
(31) Scholes, G. D.; et al. Using coherence to enhance function in chemical and biophysical systems. *Nature* **2017**, *543*, 647−656.
(32) Lee, M. K.; Bravaya, K. B.; Coker, D. F. First-Principles Models for Biological Light-Harvesting: Phycobiliprotein Complexes from Cryptophyte Algae. *J. Am. Chem. Soc.* **2017**, *139*, 7803−7814.
(33) Jumper, C. C.; Van Stokkum, I. H.; Mirkovic, T.; Scholes, G. D. Vibronic Wavepackets and Energy Transfer in Cryptophyte Light-Harvesting Complexes. *J. Phys. Chem. B* **2018**, *122*, 6328−6340.
(34) Kim, C. W.; Lee, W. G.; Kim, I.; Rhee, Y. M. Effect of Underdamped Vibration on Excitation Energy Transfer: Direct Comparison between Two Different Partitioning Schemes. *J. Phys. Chem. A* **2019**, *123*, 1186−1197.
(35) Kim, H.; Nassimi, A.; Kapral, R. Quantum-classical Liouville dynamics in the mapping basis. *J. Chem. Phys.* **2008**, *129*, 084102.
(36) Kim, H. W.; Rhee, Y. M. Improving long time behavior of Poisson bracket mapping equation: A non-Hamiltonian approach. *J. Chem. Phys.* **2014**, *140*, 184106.
(37) Scholes, G. D. Long-Range Resonance Energy Transfer in Molecular Systems. *Annu. Rev. Phys. Chem.* **2003**, *54*, 57−87.
(38) Liang, X.; Yan, Z. P.; Han, H. B.; Wu, Z. G.; Zheng, Y. X.; Meng, H.; Zuo, J. L.; Huang, W. Peripheral Amplification of Multi-Resonance Induced Thermally Activated Delayed Fluorescence for Highly Efficient OLEDs. *Angew. Chem., Int. Ed.* **2018**, *57*, 11316−11320.
(39) Nakatsuka, S.; Gotoh, H.; Kinoshita, K.; Yasuda, N.; Hatakeyama, T. Divergent Synthesis of Heteroatom-Centered 4,8,12-Triazatriangulenes. *Angew. Chem., Int. Ed.* **2017**, *56*, 5087−5090.
(40) Ahn, D. H.; Kim, S. W.; Lee, H.; Ko, I. J.; Karthik, D.; Lee, J. Y.; Kwon, J. H. Highly efficient blue thermally activated delayed fluorescence emitters based on symmetrical and rigid oxygen-bridged boron acceptors. *Nat. Photonics* **2019**, *13*, 540−546.
(41) Kim, D. Effects of Intermolecular Interactions on the Singlet−Triplet Energy Difference: A Theoretical Study of the Formation of Excimers in Acene Molecules. *J. Phys. Chem. C* **2015**, *119*, 12690−12697.
(42) Lee, K.; Kim, D. Local-excitation versus charge-transfer characters in the triplet state: Theoretical insight into the singlet-triplet energy differences of carbazolyl-phthalonitrile-based thermally activated delayed fluorescence materials. *J. Phys. Chem. C* **2016**, *120*, 28330−28336.
(43) Samanta, P. K.; Kim, D.; Coropceanu, V.; Brédas, J. L. Up-Conversion Intersystem Crossing Rates in Organic Emitters for Thermally Activated Delayed Fluorescence: Impact of the Nature of Singlet vs Triplet Excited States. *J. Am. Chem. Soc.* **2017**, *139*, 4042−4051.
(44) El-Sayed, M. A. Spin-orbit coupling and the radiationless processes in nitrogen heterocyclics. *J. Chem. Phys.* **1963**, *38*, 2834−2838.
(45) Furche, F.; Ahlrichs, R.; Hättig, C.; Klopper, W.; Sierka, M.; Weigend, F. Turbomole. *Wiley Interdiscip. Rev.: Comput. Mol. Sci.* **2014**, *4*, 91−100.
(46) Shao, Y.; et al. Advances in molecular quantum chemistry contained in the Q-Chem 4 program package. *Mol. Phys.* **2015**, *113*, 184−215.
(47) Gerenkamp, M.; Grimme, S. Spin-component scaled second-order Møller-Plesset perturbation theory for the calculation of molecular geometries and harmonic vibrational frequencies. *Chem. Phys. Lett.* **2004**, *392*, 229−235.
(48) Schirmer, J. Beyond the random-phase approximation: A new approximation scheme for the polarization propagator. *Phys. Rev. A: At., Mol., Opt. Phys.* **1982**, *26*, 2395−2416.
(49) Christiansen, O.; Koch, H.; Jørgensen, P. The second-order approximate coupled cluster singles and doubles model CC2. *Chem. Phys. Lett.* **1995**, *243*, 409−418.
(50) Friese, D. H.; Törk, L.; Hättig, C. Vibrational frequency scaling factors for correlation consistent basis sets and the methods CC2 and MP2 and their spin-scaled SCS and SOS variants. *J. Chem. Phys.* **2014**, *141*, 194106.
(51) Chai, J. D.; Head-Gordon, M. Systematic optimization of long-range corrected hybrid density functionals. *J. Chem. Phys.* **2008**, *128*, 084106.
(52) Marian, C. M. Spin-orbit coupling and intersystem crossing in molecules. *Wiley Interdiscip. Rev. Comput. Mol. Sci.* **2012**, *2*, 187−203.
(53) Tomasi, J.; Mennucci, B.; Cancès, E. The IEF version of the PCM solvation method: An overview of a new method addressed to study molecular solutes at the QM ab initio level. *J. Mol. Struct.: THEOCHEM* **1999**, *464*, 211−226.
(54) Plasser, F.; Bäppler, S. A.; Wormit, M.; Dreuw, A. New tools for the systematic analysis and visualization of electronic excitations. II. Applications. *J. Chem. Phys.* **2014**, *141*, 024107.
(55) Frigo, M.; Johnson, S. G. The design and implementation of FFTW3. *Proc. IEEE* **2005**, *93*, 216−231.
(56) Niu, Y.; Peng, Q.; Deng, C.; Gao, X.; Shuai, Z. Theory of Excited State Decays and Optical Spectra: Application to Polyatomic Molecules. *J. Phys. Chem. A* **2010**, *114*, 7817−7831.
(57) Etinski, M.; Tatchen, J.; Marian, C. M. Time-dependent approaches for the calculation of intersystem crossing rates. *J. Chem. Phys.* **2011**, *134*, 154105.

https://doi.org/10.1021/jacsau.1c00179
JACS Au 2021, 1, 987−997